Universal link of magnetic exchange and structural behavior under pressure in chromium spinels

Ilias Efthimiopoulos,[1,2,*] Indiras Khatri,[3] Zhi T. Y. Liu,[3] Sanjay V. Khare,[3] Pankaj Sarin,[4] Vladimir Tsurkan,[5] Alois Loidl,[5] Dongzhou Zhang,[6] and Yuejian Wang[1,†]

[1]*Department of Physics, Oakland University, Rochester, Michigan 48309, USA*
[2]*Deutsches GeoForschungsZentrum, Section 4.3, Telegrafenberg, 14473, Potsdam, Germany*
[3]*Department of Physics and Astronomy, University of Toledo, Toledo, Ohio 43606, USA*
[4]*School of Materials Science and Engineering, Oklahoma State University, Tulsa, Oklahoma 74106, USA*
[5]*EP V, Center for Electronic Correlations and Magnetism, University of Augsburg, 86159 Augsburg, Germany*
[6]*Partnership for Extreme Crystallography, University of Hawaii at Manoa, Honolulu, Hawaii 96822, USA*

(Received 7 November 2017; revised manuscript received 14 May 2018; published 31 May 2018)

We have conducted high-pressure x-ray diffraction studies on the $MnCr_2O_4$ and $NiCr_2O_4$ spinels at room temperature. Both compounds undergo pressure-induced structural transitions into diverse tetragonal modifications. Based on these experimental observations and our *ab initio* calculations, we show that the Cr-oxide spinels with magnetic A^{2+} cations (A^{2+} = Mn, Fe, Co, Ni) follow a similar trend as their chalcogenide counterparts with nonmagnetic A^{2+} ions, i.e., the transition pressure is proportionally related with the magnitude of the Cr-Cr magnetic exchange interactions. Therefore, we reach the conclusion that the Cr-Cr magnetic exchange interactions alone suffice to account for the high-pressure behavior of these systems. Our results clearly depict the close relationship between the structural and magnetic degrees of freedom in Cr-bearing spinels.

DOI: 10.1103/PhysRevB.97.184435

I. INTRODUCTION

The series of $A^{2+}Cr^{3+}{}_2X_4$(A^{2+} = Mn-Zn, Cd, Hg; X = O, S, Se) spinels (SG $Fd\bar{3}m$, $Z = 8$) constitutes an ideal system for studying magnetic exchange interactions in solids [1–3]. The spinel structure is composed of edge-sharing Cr^{3+} octahedral units with six nearest neighbors/anions (the Cr^{3+} cations themselves form tetrahedra in a pyrochlore-type lattice, thus allowing for magnetic frustration) and relatively "isolated" A^{2+} tetrahedral units with four nearest neighbors (Fig. 1).

Depending on the type and size of the tetrahedrally coordinated A^{2+} cations and the corresponding anions, the magnetic exchange interactions can vary significantly [3,4]. As established already in the 1960s [5–8], spinels with nonmagnetic A^{2+} cations may exhibit either direct Cr^{3+}-Cr^{3+} antiferromagnetic (AFM) or indirect ferromagnetic (FM) Cr-X-Cr interactions depending on the Cr^{3+}-Cr^{3+} distance. The AFM interactions are dominant in the Cr-spinel oxides with smaller Cr^{3+}-Cr^{3+} distances; on the other hand, the Cr-X-Cr FM exchange prevails in the Cr-bearing sulfide and selenide spinel series due to the larger Cr^{3+}-Cr^{3+} separation distances compared to the oxides [6,8–10]. This fact alone indicates the strong coupling between magnetism and structure in these compounds. Indeed, several experimental studies have shown the enhancement of the AFM interactions upon decreasing the Cr^{3+}-Cr^{3+} distances, via the reduction of the Cr-spinel volume under external compression [11,12]. In certain cases, electronic changes, e.g., insulator-to-metal [13–16] or semiconductor-to-semiconductor [17] transitions, have been reported. On the other hand, the magnetic interactions of the oxide spinels with magnetic A^{2+} cations are more complex, since one needs to consider also the A^{2+}-Cr^{3+} and the more distant A^{2+}-A^{2+} magnetic exchange interactions for interpreting accurately the respective magnetic ground states [2,4,18].

In previous works we have unraveled the close correlation between the magnetic exchange interactions and the pressure-induced structural transitions in ACr_2X_4 Cr-spinel chalcogenides with nonmagnetic A^{2+} cations (A = Zn, Cd, Hg; X = S, Se) [19,20]. In particular, we have shown that the ratio of the next-nearest-neighbor (K_{nnn}) over the nearest-neighbor (J_{nn}) magnetic interactions is proportional to the structural transition pressure (P_{Tr}) from the starting cubic $Fd\bar{3}m$ phase toward a tetragonal modification [21,22]. Notable exceptions from this trend are $ZnCr_2Se_4$ [23] and $CuCr_2Se_4$ [24], as their high-pressure behavior appears to be dictated by the similar ionic radii of tetrahedrally coordinated Zn^{2+} and Cu^{2+} with the octahedrally coordinated Cr^{3+}, and the higher covalency of the larger-sized Se anions (for a more detailed discussion see Ref. [24]). Here we expand this idea to Cr-oxide spinels with magnetic A^{2+} cations (A^{2+} = Mn-Cu). For this purpose, we have investigated the high-pressure structural behavior of $MnCr_2O_4$ and $NiCr_2O_4$ spinels by means of x-ray diffraction (XRD) and density functional theory (DFT)-based calculations. Combined with results from the literature, we could find a clear correlation between the Cr-Cr magnetic exchange interactions and P_{Tr} in these systems, as we describe below.

II. EXPERIMENTAL AND COMPUTATIONAL DETAILS

The $MnCr_2O_4$ and $NiCr_2O_4$ single-crystalline samples have been synthesized with solid-state reaction, as reported elsewhere [25,26]. The high-pressure sample environment was generated by rhenium gasketed diamond-anvil cells, equipped

*ilias.efthymiopoulos@gfz-potsdam.de
†ywang235@oakland.edu

 ©2018 American Physical Society

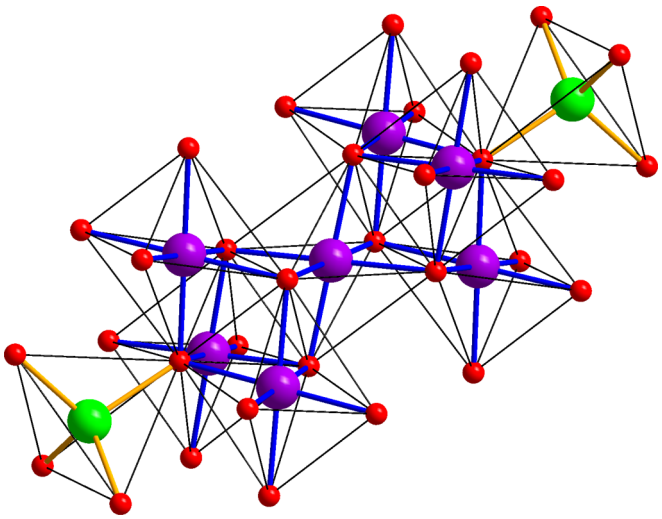

FIG. 1. Crystal structure of the $A^{2+}Cr^{3+}{}_2O_4$ spinel compounds (A^{2+} = Mn-Zn, Cd, Hg). The A, Cr, and oxygen atoms are shaded in green, purple, and red, respectively.

with diamonds of 300-μm culet diameter. The ruby luminescence method was employed for pressure calibration [27]. The angle-resolved high-pressure powder XRD measurements were performed at the 16BM-D beamline of the High Pressure Collaborative Access Team ($MnCr_2O_4$), and the 13-BMC beamline of the GeoSoilEnviroCARS ($NiCr_2O_4$) at the Advanced Photon Source of Argonne National Laboratory [28]. The incident monochromatic x-ray beam energies were E = 29.2 keV ($\lambda = 0.4246$ Å, $MnCr_2O_4$) and $E = 28.6$ keV ($\lambda = 0.434$ Å, $NiCr_2O_4$). Helium served as a pressure-transmitting medium in both experiments.

The majority of the measured XRD patterns were fitted with the Rietveld method. The refined parameters in each case were the lattice parameters, the atomic coordinates (Mn, Ni, and Cr reside in fixed positions in the ambient-pressure structures), and the profile parameters of the Stephens peak function [29], whereas the background was modeled with a Chebyshev polynomial. Since the diffractograms showed textured rings, we employed a spherical harmonics correction [30] in order to account for the preferred orientation of the powder particles.

Our DFT-based calculations have been performed with the Vienna *Ab initio* Simulation Package (VASP) [31–34], using projector-augmented wave method [35,36] with the Perdew-Burke-Ernzerhof generalized gradient approximation (GGA) [37]. The GGA + U correction scheme was used for the d orbitals of Mn, Ni, and Cr. The U values were chosen to be 3.9 eV for Mn, 6.2 eV for Ni, and 3.7 eV for Cr [38,39]. Plane-wave basis with appropriate k-point meshes and Gaussian smearing was used. We carefully constructed the cells with various magnetic configurations, including random solid solutions [40,41] provided in the Alloy Theoretic Automated Toolkit (ATAT) [42,43]. In each run the cell shape and atomic positions were allowed to freely relax as in earlier works [23,44,45]. To determine the magnetic exchange interactions parameters, we have calculated the total energies of various different magnetic configurations. Detailed quantitative descriptions of the above computational methods are provided in Supplemental Material [46].

III. RESULTS AND DISCUSSION

A. Cubic $MnCr_2O_4$ under pressure

In Fig. 2(a) we present XRD patterns of $MnCr_2O_4$ at selected pressures. At ambient conditions, $MnCr_2O_4$ crystallizes in the cubic spinel $Fd\bar{3}m$ structure (Fig. 1). This ambient-pressure phase is retained up to ~8 GPa. Above this pressure, an abrupt broadening of the $Fd\bar{3}m$ Bragg peaks is evidenced, as revealed by a change in the pressure dependence of the respective widths (Fig. S1 in Supplemental Material [46]). Since we have used helium as pressure-transmitting medium, we can most likely exclude nonhydrostatic effects at this relatively low pressure range [47]. Due to this Bragg-peak broadening, the $Fd\bar{3}m$ phase does no longer reproduce the XRD patterns satisfactorily; a tetragonal structure, on the other hand, can reasonably index the measured diffractograms (Fig. S1 [46]). We note that upon passing from the cubic to the tetragonal structure, the majority of the $Fd\bar{3}m$ Bragg peaks split into two or more components, thus accounting for the observed abrupt width broadening (Fig. S1 [46]). Hence, we conclude that a cubic→tetragonal distortion takes place in $MnCr_2O_4$ close to 8.3 GPa, similar to $CoCr_2O_4$ [45]. Due to this Bragg-peak broadening, we could not assign a unique space group for this high-pressure tetragonal phase.

Further compression results in the appearance of a shoulder band in the Bragg peak located at ~8° close to 21 GPa [Fig. 2(a)]. This shoulder becomes more prominent with increasing pressure, at the expense of its adjacent Bragg peak. This observation is interpreted as a second structural transition, initiating at 21 GPa and completed at ~30 GPa [Fig. 2(a)]. This second high-pressure phase can be also indexed to a tetragonal structure, with its c axis reduced by 7.5% and its a axis expanded by 4% compared to the first high-pressure tetragonal phase (Table S1 in Supplemental Material [46]). Again, due to the Bragg-peak broadening, we could not assign a unique space group for this second high-pressure tetragonal phase. Further compression above 34 GPa appears to lead to an orthorhombic distortion (not shown); the pronounced broadening of the Bragg peaks, however, does not allow for reliable XRD refinements beyond that pressure.

Due to the aforementioned Bragg-peak broadening of our XRD patterns, we performed mostly Le Bail refinements for the majority of the $MnCr_2O_4$ diffractograms. In Fig. 2(b) we plot the axial ratio of the tetragonal high-pressure phases of $MnCr_2O_4$; the respective lattice parameters are provided in Table S1 [46]. We can clearly observe that the cubic→tetragonal distortion is accompanied by a slight deviation from the cubic c/a unity value. On the other hand, the second pressure-induced tetragonal→tetragonal transition is manifested by an abrupt drop of the c/a axial ratio, owing to the sudden reduction of the tetragonal c axis at the transition point (Table S1 [46]). Such behavior is reminiscent of the documented pressure-induced structural transitions in several Cr-bearing spinels [20,48]. Nevertheless, both of the pressure-induced $MnCr_2O_4$ structural transitions do not show any sizable volume changes at the respective transition points [Fig. 2(c)]. The experimental P-V data were fitted with Birch-Murnaghan equations of state [49,50], with the respective results tabulated in Table I.

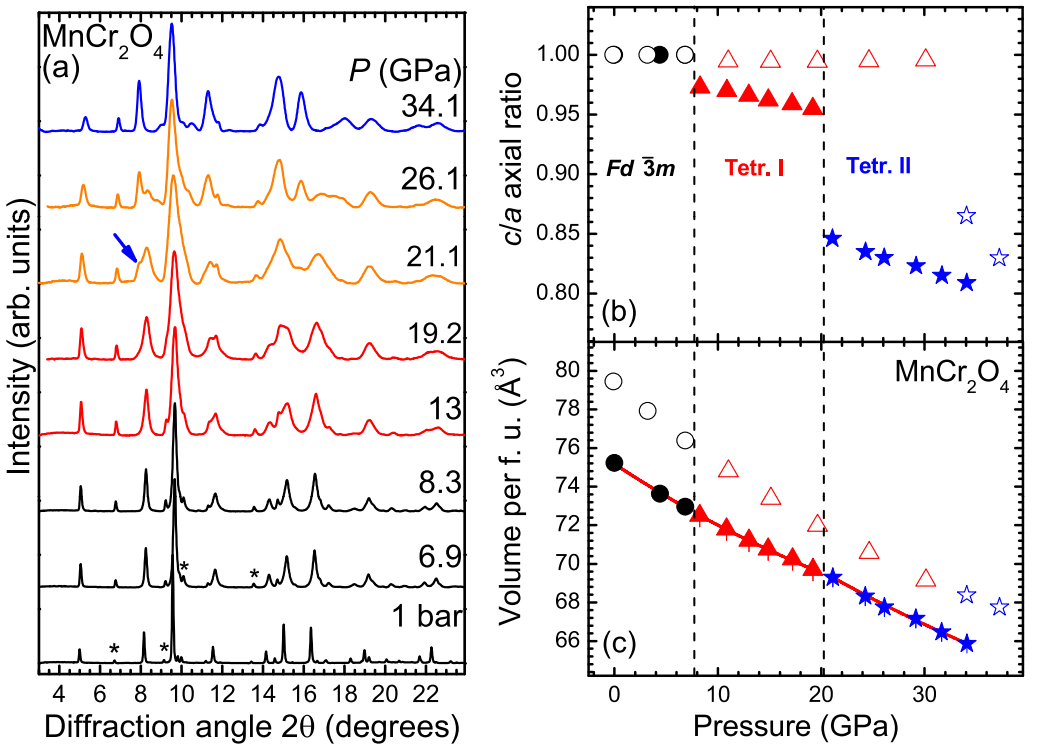

FIG. 2. (a) Selected XRD patterns of $MnCr_2O_4$ at various pressures ($T = 300$ K, $\lambda = 0.4246$ Å). The various phases are distinguished by black ($Fd\bar{3}m$), red (HP-tetragonal I), and blue (HP-tetragonal II) colors. Orange diffractograms denote the coexistence range. Asterisks mark the strongest Bragg peaks of the Cr_2O_3 secondary phase. We also plot the (b) c/a axial ratio and (c) volume per formula unit (f.u.) as a function of pressure for all phases of $MnCr_2O_4$ (error bars lie within the symbols). The closed and open symbols correspond to experimental and DFT data, respectively. The vertical dashed lines depict the experimental transition pressures, and the red solid lines through the symbols indicate the fitted Birch-Murnaghan equations of state [49,50]. Black circles, red triangles, and blue stars correspond to the $Fd\bar{3}m$, the tetragonal AFM-MnCr, and the tetragonal AFM-Cr phases of $MnCr_2O_4$, respectively, in both panels. The obtained elastic parameters are listed in Table I. The respective lattice parameters are provided in Tables S1 and S2 [46].

In order to understand the origin behind these pressure-induced structural transitions, we have performed DFT calculations on $MnCr_2O_4$ assuming a paramagnetic (PM) cubic structure and two different tetragonal AFM configurations, one with Mn spin-up and parallel to each Mn cation and Cr spin-down aligned parallel to each Cr cation but antiparallel to the Mn ones (similar to the experimental observation at ambient pressure [51]), and one with all Mn^{2+} in spin-up states, and half of Cr^{3+} in the same plane on the c axis with spin-up states, the other half spin-down as in $CoCr_2O_4$ [45] called AFM-MnCr

TABLE I. Elastic parameters (volume V_{Tr}, bulk modulus B_{Tr}, and the pressure derivative of bulk modulus B'_{Tr}) for the various phases of $MnCr_2O_4$ and $NiCr_2O_4$, as obtained by Birch-Murnaghan equations of state [49,50]. Each parameter is evaluated at the transition pressure point P_{Tr}. N/A: not available.

Phase		P_{Tr} (GPa)	V_{Tr}/Z(Å^3)	B_{Tr} (GPa)	B'_{Tr}
$MnCr_2O_4$	Exp.	10^{-4}	75.2 (exp.)	212(5)	4 (fixed)
$Fd\bar{3}m$	DFT (ParaM)		79.4	164.6	3.9
	Exp. [53]		75.5	180	N/A
$MnCr_2O_4$	Exp.	8.3	72.5 (exp.)	230(6)	5.3(3)
HP1	DFT (AFM-MnCr)	17	72.8	164.1	4.5
$MnCr_2O_4$	Exp.	21.1	69.3 (exp.)	231(3)	4 (fixed)
HP2	DFT (AFM-Cr)	30.5	69.5	164.3	3.9
$NiCr_2O_4$	Exp.	10^{-4}	71.9 (exp.)	183(1)	4 (fixed)
$I4_1/amd$	DFT (ParaM)		73.9	165.3	3.3
	DFT (AFM)		75.5	166.5	3.6
$NiCr_2O_4$	Exp.	19.4	64 (exp.)	182(6)	4.9(6)
$P4_32_12$	DFT (ParaM)	28.0	62.5	154.7	3.7
	DFT (AFM)	32.0	61.2	146.0	4.4

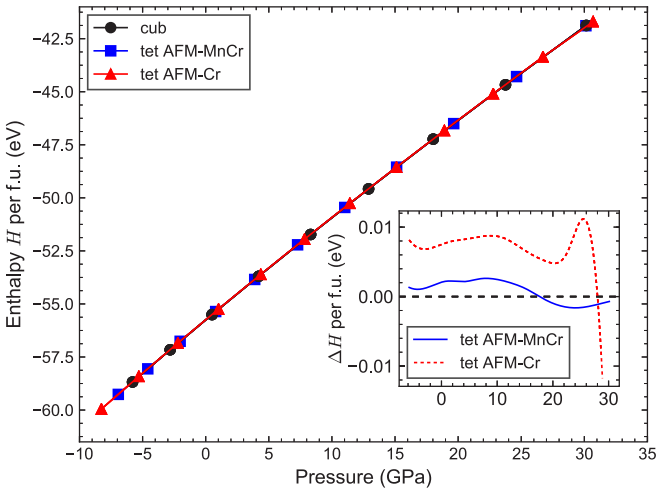

FIG. 3. Calculated enthalpies of the cubic paramagnetic (black), the tetragonal AFM1 (AFM-MnCr, blue), and tetragonal AFM2 (AFM-Cr, red) phases as a function of pressure. Inset: the enthalpy difference between the tetragonal AFM1 and AFM2 phases and the cubic phase with respect to pressure. Enthalpy H is defined as $H(P) = E + PV$, and a lower value of H indicates the phase stability. The cubic→AFM-MnCr transition is calculated at 17 GPa (experimental value is 8.3 GPa). The AFM-MnCr→AFM-Cr transition is expected to take place at 30.5 GPa (extrapolated in Fig. S2 in Supplemental Material [46], the experimental value is 21.1 GPa).

and AFM-Cr, respectively (Tables S2 and S3 [46]). From our calculations, we could find that the cubic→AFM-MnCr and the AFM-MnCr→AFM-Cr transitions take place at 17 and 30.5 GPa, respectively (Fig. 3 and Fig. S2 [46]). Even though the experimental and calculated transition pressures exhibit discrepancies in their values, owing partially to the fact that DFT calculations are performed at 0 K and not at room temperature as the experiments, as well as the overestimation of the lattice parameters within the GGA used here (see, e.g., Ref. [52]), we are confident that we have captured the main features of the observed $MnCr_2O_4$ pressure-induced structural transitions, i.e., that both structural transitions are accompanied/triggered by changes in the magnetic properties of $MnCr_2O_4$. We will return back to this point later.

Despite the aforementioned transition pressure discrepancies, the calculated lattice parameters, c/a axial ratios, and the P-V data for the various phases of $MnCr_2O_4$ are qualitatively very similar to their experimental counterparts [Figs. 2(b) and 2(c)]. We can immediately observe that the DFT-calculated values lie always higher than their experimental counterparts, attributed to the tendency of the GGA approximation used here to overestimate the unit-cell volumes and, concomitantly, underestimate the bulk moduli [52].

B. Compression of Jahn-Teller active tetragonal $NiCr_2O_4$

Turning now to the high-pressure structural behavior of $NiCr_2O_4$, selected XRD patterns at various pressures are shown in Fig. 2(b). At ambient conditions, $NiCr_2O_4$ adopts a tetragonal $I4_1/amd$ structure ($Z = 4$), a direct subgroup of the $Fd\bar{3}m$ phase [54], given the Ni^{2+} Jahn-Teller active ions [55]. Compression leads to changes in the XRD patterns starting at 19.4 GPa, with the most notable difference being the vanishing of the intense Bragg peak at 10.4° [Fig. 4(a)]. Therefore, it is obvious that $NiCr_2O_4$ has undergone a structural transition at 19.4 GPa. Indexing of the high-pressure $NiCr_2O_4$ modification led to another tetragonal structure with SG $P4_32_12$ ($Z = 8$) [Fig. 4(b)]. The $I4_1/amd \rightarrow P4_32_12$ transition does not involve any cationic coordination increase for either Ni^{2+} or Cr^{3+} (SG $P4_32_12$ is a subgroup of SG $I4_1/amd$). Even though such phase has been observed as a low-temperature modification of $MgTi_2O_4$ [56], this is one of the rare reports of a Cr-bearing spinel adopting this particular tetragonal structure.

The high quality of the XRD patterns allowed for Rietveld refinements of the $NiCr_2O_4$ diffractograms. The respective lattice parameters and atomic coordinates are provided in Table S4 [46]. Here we show the tetragonal c/a axial ratio and the P-V data for the two $NiCr_2O_4$ phases (Fig. 5). As we can observe in Fig. 5(a), the tetragonal c/a axial ratio increases upon compression, indicating the enhancement of the Jahn-Teller polyhedral distortion in the $NiCr_2O_4$ $I4_1/amd$ ambient-pressure structure. We note here that the $I4_1/amd$ symmetry dictates one single Ni–O bond distance in the NiO_4 tetrahedra, and two Cr–O bond distances in the CrO_6 octahedra (two apical bonds along the long c axis, and two equatorial bonds parallel to the tetragonal ab plane) comprising the tetragonal spinel phase. Thus, the increase of the c/a ratio directly implies the elongation of the CrO_6 octahedra along the c axis, i.e., the apical Cr–O bonds are increasing at the expense of the equatorial ones, in excellent agreement with our refined Cr-O data (Table S4 [46]). Nevertheless, the overall Jahn-Teller distortion in the starting $NiCr_2O_4$ $I4_1/amd$ phase is small and is virtually eliminated upon compression, as revealed by the pressure-induced evolution of the Jahn-Teller distortion parameter σ_{JT}, as in the case of $CuWO_4$ [57,58] (Fig. S3 [46]).

Upon passing into the high-pressure $P4_32_12$ phase, we can observe that the c/a ratio decreases by ∼2% due to the abrupt reduction of the c axis (Fig. 5(a) and Table S4 [46]), resulting also in a ∼3% volume change at the $I4_1/amd \rightarrow P4_32_12$ transition point [Fig. 5(b)], thus classifying the transition as of first order. We can also notice that the pressure-induced c/a trend reverses in the $P4_32_12$ phase, i.e., the equatorial Cr–O bonds expand at the expense of the apical ones. The latter observation indicates that (a) the Jahn-Teller distortion caused by the Ni^{2+} ions persists also in the high-pressure phase, contrary to the general trend of eliminating the Jahn-Teller effect upon sufficient compression [59], and (b) the overall polyhedral distortion in the high-pressure $P4_32_12$ modification is opposite to the starting $I4_1/amd$ one. Plotting of the Jahn-Teller distortion parameter σ_{JT} shows that the Jahn-Teller distortion increases one order of magnitude in the $P4_32_12$ phase at the transition point (Fig. S3 [46]). Further compression enhances the CrO_6 polyhedral distortion, whereas a downturn in the pressure slope of σ_{JT} is detected close to 36–40 GPa. Extrapolation of the respective data indicates the complete Jahn-Teller suppression at ∼120 GPa. Given the discussion that follows below, we tend to attribute the enhancement of the Jahn-Teller distortion upon the $I4_1/amd \rightarrow P4_32_12$ transition not as the driving force behind the observed structural change, as e.g. in the case of $CuWO_4$ [57,58], but rather as a *byproduct* of the magnetic changes accompanying the structural modification.

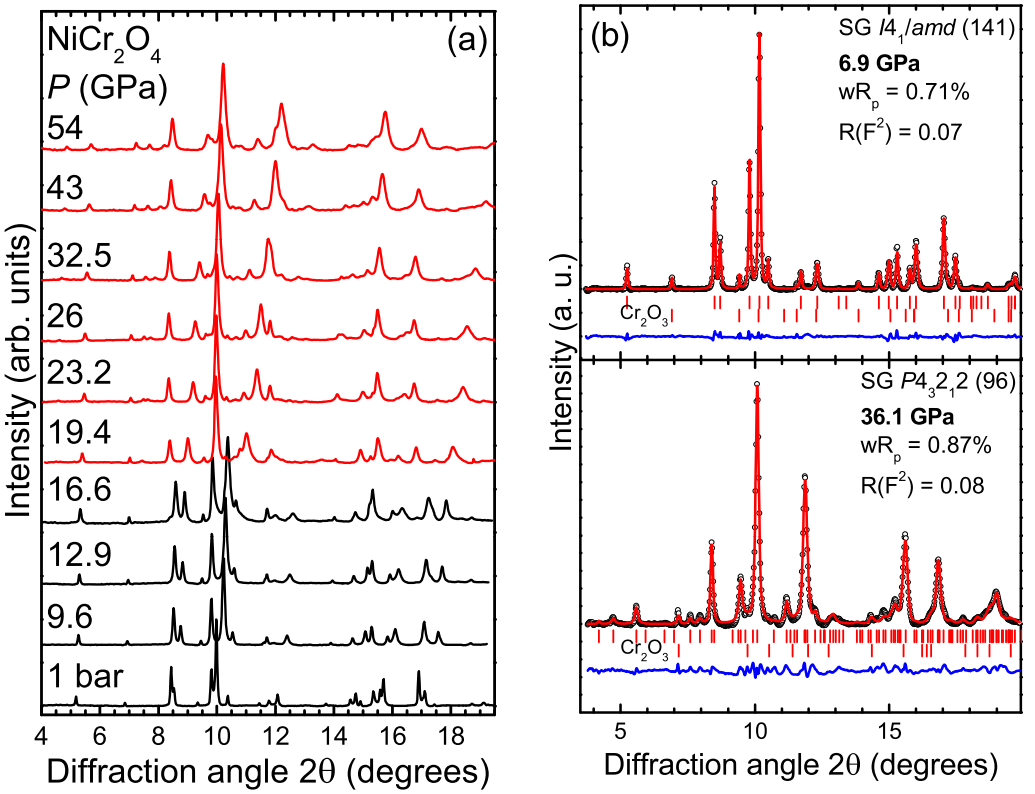

FIG. 4. (a) Selected XRD patterns of $NiCr_2O_4$ at various pressures ($T = 300$ K, $\lambda = 0.4340$ Å). The various phases are distinguished by black ($I4_1/amd$) and red ($P4_32_12$) colors. (b) Examples of Rietveld refinements of $NiCr_2O_4$ XRD patterns at 6.9 GPa (top) and at 36.1 GPa (bottom). Dots stand for the measured spectra, the red solid lines represent the best refinements, and their difference is drawn as blue lines. Vertical ticks mark the respective Bragg-peak positions.

In Fig. 5(b) we plot the experimental and calculated P-V data for both phases. We can immediately observe that the DFT-calculated values always lie higher than their experimental counterparts, attributed to the tendency of the GGA approximation used here to overestimate the unit-cell volumes and, concomitantly, underestimate the bulk moduli [52]. Interestingly, we note that the experimental bulk modulus of the high-pressure $P4_32_12$ phase is similar to the bulk modulus value of the starting $I4_1/amd$ structure, implying a smaller bulk modulus for $P4_32_12$, i.e., the high-pressure phase of $NiCr_2O_4$ appears to be *softer* than the ambient-pressure structure; this is more evident in our DFT calculations (Table I). Even though such effect is quite *unusual* in high-pressure studies, a possible cause might be underlying electronic effects due to changes in the nature of interionic bonding after the $I4_1/amd \rightarrow P4_32_12$ transition (e.g., the Cr-O distances expand by ~6%, whereas the Ni–O bond lengths shorten by ~8% at the transition point), as in the case of CrN [60].

Our DFT calculations in the case of $NiCr_2O_4$ were performed assuming a PM and AFM $I4_1/amd$ structures, as well as a PM and an AFM high-pressure $P4_32_12$ phase (Table S5 [46]). Evaluation of the respective enthalpies indicates that the AFM $I4_1/amd$ structure adopts the PM $P4_32_12$ phase close to 25 GPa (Fig. 6), in good agreement with the experimental value, whereas the PM $I4_1/amd$ phase transforms into the PM $P4_32_12$ phase close to 35 GPa (the AFM $P4_32_12$ phase is adopted in both cases 5 GPa higher than the PM one; Fig. 6 and Fig. S3 [46]). However, from the reasons reported earlier regarding the temperature effect, as well as the overestimation of the volume within the GGA approximation, it appears that the calculated transition pressure depends also on the choice of the exact magnetic configuration. The latter enlightens the inconsistencies in the experimental and calculated transition pressures in the case of $MnCr_2O_4$, as we discuss in more detail in the next section.

C. Pressure-induced structural transition and magnetic exchange in Cr spinels

Having established the transition pressures (P_{Tr}) for both $MnCr_2O_4$ and $NiCr_2O_4$ spinels, we turn now to some common aspects of the (first) pressure-induced structural transition in the Cr-spinel series. Comparison of the available literature reveals that for sulfide and selenide Cr spinels, the cubic→tetragonal transition is always accompanied by a volume decrease of 4–5% at the transition point [19–23,61]. In addition, DFT calculations have identified concomitant magnetic changes accompanying these structural transitions, i.e., from the starting FM states toward AFM ones [20–22]. Taken together, we were able to identify a linear relationship between the P_{Tr} of Cr-bearing spinel sulfides and selenides and the K_{nnn}/J_{nn} ratio of next-nearest-neighbor K_{nnn} to nearest-neighbor J_{nn} Cr^{3+} magnetic exchange interactions [19,20].

Given, however, that the K_{nnn} interactions are not relevant for Cr-oxide spinels bearing magnetic A^{2+} cations [2,4,18], does a similar relation between P_{Tr} and magnetic exchange

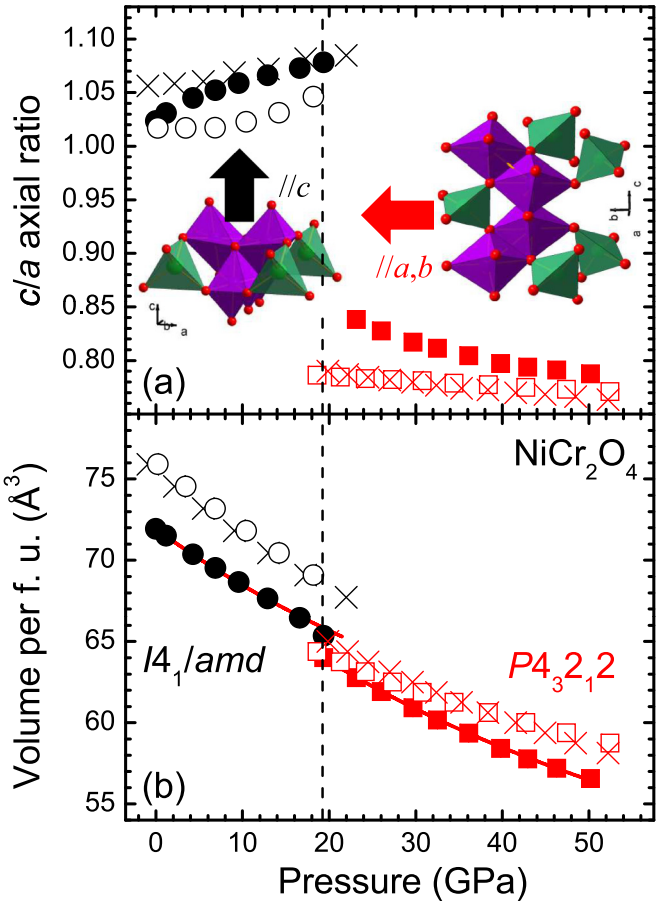

FIG. 5. Plot of the (a) c/a axial ratio and (b) volume per f.u. as a function pressure for the two modifications of $NiCr_2O_4$ (error bars lie within the symbols). The closed and open symbols correspond to experimental and DFT data, respectively. The vertical dashed lines depict the experimental transition pressures, and the red solid lines through the symbols indicate the fitted Birch-Murnaghan equations of state [49,50]. Nomenclature of the symbols is as follows: Black circles and red squares correspond to the PM $I4_1/amd$ and $P4_32_12$ phases of $NiCr_2O_4$, respectively. The black and red (X) symbols stand for the corresponding AFM $I4_1/amd$ and $P4_32_12$ phases of $NiCr_2O_4$, respectively, as obtained from DFT calculations. The obtained elastic parameters are listed in Table I. The respective lattice parameters are provided in Tables S4 and S5 [46]. The overall deformation of the $NiCr_2O_4$ polyhedra is also drawn for clarity in panel (a).

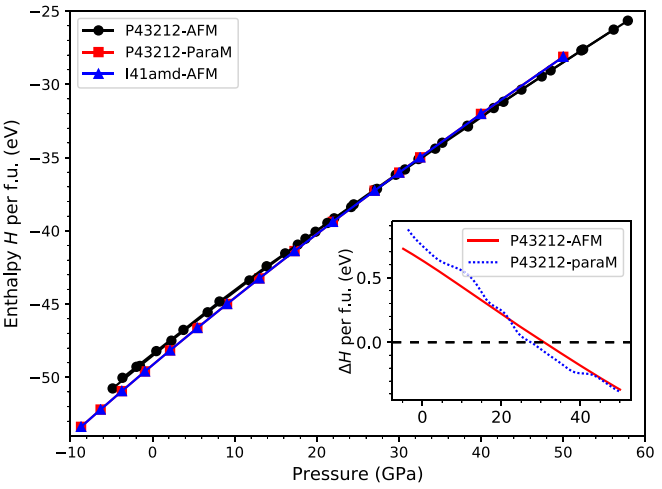

FIG. 6. Calculated enthalpies of the $I4_1/amd$ (AFM, blue), the $P4_32_12$-AFM (black), and the $P4_32_12$-ParaM (red) $NiCr_2O_4$ phases as a function of pressure. Inset: the enthalpy difference between the $P4_32_12$ (AFM and paraM) and $I4_1/amd$ (AFM) phases with respect to pressure. Enthalpy H is defined as $H(P) = E + PV$, and a phase is stable if it has a lower value of H. The $I4_1/amd$-AFM $\rightarrow$ $P4_32_12$-ParaM transition takes place at 25 GPa, whereas the $I4_1/amd$-AFM $\rightarrow$ $P4_32_12$-AFM transition is estimated at 30 GPa.

interactions hold for these materials? For this purpose, we have calculated the relevant magnetic exchange parameters J_{AA}, J_{BB}, and J_{AB} for the whole spinel series with magnetic A^{2+} cations ($A^{(2+)}$ = Mn-Cu) at ambient pressure, the most important magnetic parameters in these compounds [4,18]. All of these data, alongside relevant literature values [4,18,62,63], are listed in Table S8 [46]. We note that J_{AA} represents the interactions between A^{2+} cations, J_{AB} denotes the magnetic exchange between A^{2+} and Cr^{3+}, and J_{BB} stands for Cr^{3+}-Cr^{3+} interactions.

In Fig. 7 we plot the calculated J_{BB} exchange parameter as a function of P_{Tr} for all the relevant spinels. We can immediately observe a linear dependence of the two parameters with the exception of $CuCr_2O_4$, which undergoes an isostructural transition at $P_{Tr} = 25$ GPa, most likely resulting from pressure-induced orbital reorientation [24]. We note also that the calculated magnetic exchange interactions of $CuCr_2O_4$ are much larger compared to the rest of the spinels (Table S8 [46]), possibly accounting for the absence of any structural transition up to 50 GPa [24]. On the other hand, $CoCr_2O_4$ undergoes a structural distortion at about 16 GPa, attributed to magnetic frustration [45]. Moreover, $FeCr_2O_4$ has been studied

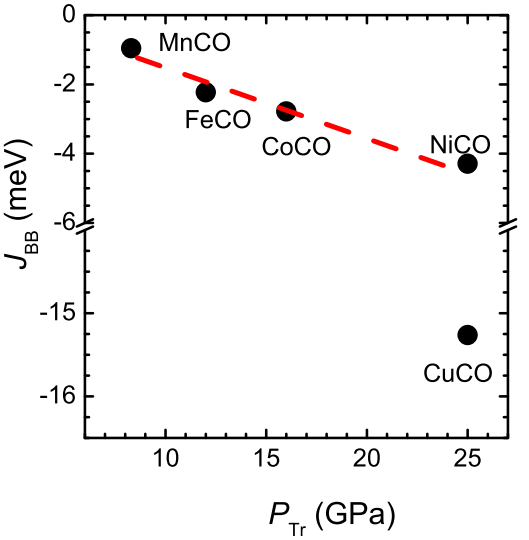

FIG. 7. Plot of the J_{BB} magnetic exchange interaction against the transition pressure P_{Tr} for the Cr spinels with magnetic A^{2+} cations. The compound abbreviations are as follows: $MnCr_2O_4$ $\rightarrow$ MnCO, $FeCr_2O_4$ $\rightarrow$ FeCO, $CoCr_2O_4$ $\rightarrow$ CoCO, $NiCr_2O_4$ $\rightarrow$ NiCO, and $CuCr_2O_4$ $\rightarrow$ CuCO (Table S8 [46]).

up to 93 GPa [64,65]. These studies established an $Fd\bar{3}m \rightarrow I4_1/amd$ structural transition close to 12 GPa in $FeCr_2O_4$ due to Jahn-Teller effects. Further compression leads to Fe↔Cr intercationic site exchange and a high-spin to low-spin state transition of divalent Fe [64]. We should also note here that the P_{Tr} of several ternary AB_2X_4 compounds was shown to depend on the cationic radii ratio of the respective constituent ions [66,67]; such relationship, however, does not seem to hold for Cr-bearing spinels (see Fig. 10 in Ref. [20]).

From our plot (Fig. 7) it becomes immediately evident that the structural distortions/transitions observed in the Cr-spinel series are closely interrelated to magnetic rather than steric or Jahn-Teller effects. Considering our aforementioned results on spinel sulfides and selenides with nonmagnetic A^{2+} cations, we can generally state at this point that the structural transitions in Cr-based spinels are intimately connected with the Cr-Cr magnetic exchange interactions.

In order to link our suggestion with the theory developed by Lyons, Kaplan, Dwight, and Menyuk (LKDM) for these systems [2], the magnetic ground state and/or the magnetic frustration of a cubic-spinel compound can be described by the parameter u:

$$u = \frac{4J_{BB}S_B}{3J_{AB}S_A}, \tag{1}$$

where S_A and S_B denote the spin magnitude of the A and B cations in the AB_2X_4 spinel phase [68]. It is clear that the parameter u represents the relative strength between the two different nearest-neighbor interactions J_{BB} and J_{AB}. According to LKDM, the numerical value of u describes the magnetic ground state of the spinel, with $u \leqq 8/9$ denoting a collinear AFM Néel state (e.g., all A-site spins parallel to each other and antiparallel to the B-site spins), $8/9 < u < 1.298$ a ferrimagnetic spiral configuration, whereas for $u > 1.298$ the latter ferrimagnetic configuration becomes unstable, resulting in an unstable spiral state. Therefore, it becomes clear that the larger the magnitude of u, the more magnetically unstable the respective spinel becomes. Given that the J_{BB} coupling constant displays a larger enhancement under pressure compared to J_{AB} (Fig. 8; see also Table I in Ref. [45]), we can reasonably anticipate the enhancement of the magnetic instability in these systems under compression. Consequently, it appears that this built-up pressure-induced magnetic instability is partially relieved by structural transitions in these materials, leading possibly also to the realization of new magnetic ground states [20,45,64].

Indeed, our DFT calculations have revealed that the structural transitions may be accompanied by magnetic ones in both $MnCr_2O_4$ and $NiCr_2O_4$ spinels. Regarding the former, we mentioned earlier the discrepancies between the experimental and calculated P_{Tr} for the observed structural transitions. Considering the sensitivity of the calculated enthalpy on the choice of the exact magnetic configuration (see the $NiCr_2O_4$ discussion earlier), one possible explanation behind the P_{Tr} discrepancies might be that the selected tetragonal AFM-MnCr and AFM-Cr states might not be the most suitable candidates for describing the $MnCr_2O_4$ magnetic configurations in the respective high-pressure tetragonal structures. More complex magnetic ground states with tetragonal symmetries might be needed for this purpose, a task which lies beyond the scope of the present paper.

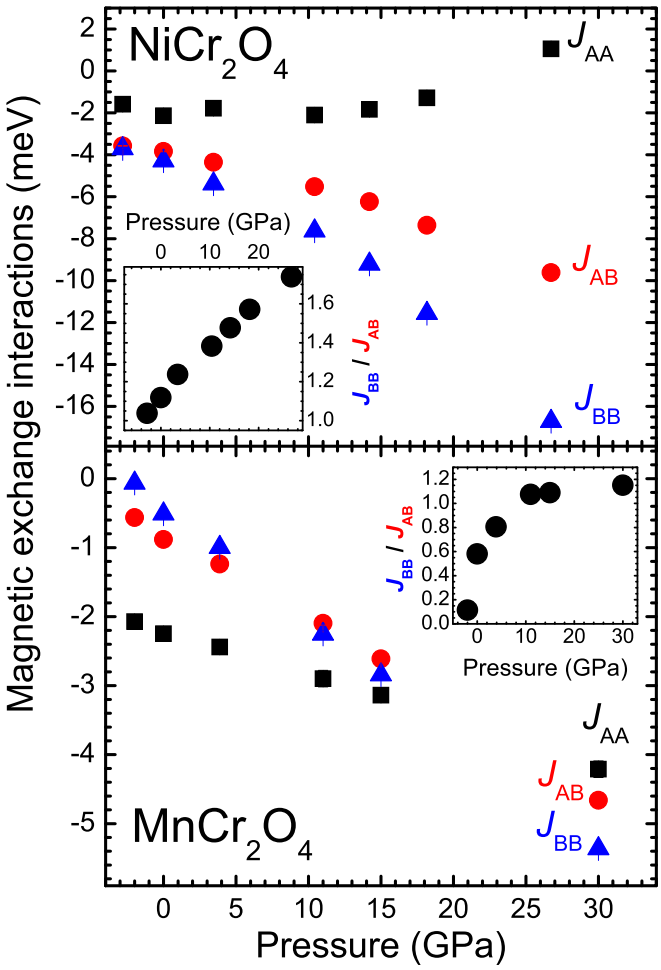

FIG. 8. Plot of the various magnetic exchange interactions for the ambient-pressure cubic and tetragonal $MnCr_2O_4$ (bottom) and $NiCr_2O_4$ (top) as a function of pressure. Even though the respective pressure stability fields of the original phases are up to ~8 and ~20 GPa, respectively, we have expanded the calculations to higher pressures for clarity. The insets depict the respective J_{BB}/J_{AB} ratios.

Finally, we consider it interesting to compare the present results on Cr spinels with the recent high-pressure studies conducted on the $A^{2+}V_2O_4$ spinels (A^{2+} = Mg, Mn, Fe, Co, Zn, Cd) [11,53]. Compared to the Cr^{3+}-bearing oxospinels with localized $3dt_{2g}$ electrons (Cr^{3+} $3d^3$; $S = 3/2$) and large electronic band gaps, the V^{3+}-bearing spinels (V^{3+} $3d^2$; $S = 1$) are closer to a localized-itinerant transition under compression [11,69]. Interestingly, such an electronic transition was speculated to take place at a critical intermetallic separation distance R_c between the Cr^{3+}-Cr^{3+} ($R_c = 2.84$ Å) and the V^{3+}-V^{3+} ($R_c = 2.97$ Å) cations [5,70]. For the V^{3+} spinels, however, the proposed R_c appears to be overestimated [53]. This appears to be the case also for the Cr-bearing oxospinels, as, e.g., the intermetallic Cr^{3+}-Cr^{3+} distance in $CoCr_2O_4$ reaches $R_c = 2.84$ Å close to 30 GPa, but without any indication of a metallic transition [45]. Moreover, the high-pressure $P4_32_12$ modification of $NiCr_2O_4$ exhibits an intermetallic Cr^{3+}-Cr^{3+} distance of 2.6 Å close to 50 GPa, again with no indication

of metallization (at least visually). Hence, the concept of a critical intermetallic separation distance leading to localized-to-itinerant transitions in transition-metal compounds should be revisited.

IV. CONCLUSIONS

In summary, we have investigated the high-pressure structural behavior of the $MnCr_2O_4$ and $NiCr_2O_4$ spinels at room temperature. In both cases, we have unraveled pressure-induced structural transitions into tetragonal modifications. In the case of $MnCr_2O_4$, the structural transitions did not result in sizable volume changes at the respective transition points. On the other hand, $NiCr_2O_4$ undergoes a first-order $I4_1/amd \rightarrow P4_32_12$ transition with a reversal of the c/a axial ratio slope, indicating opposite Jahn-Teller effects in the two structures.

Considering the present results, as well as the available literature, we have shown that the Cr-oxide spinels with magnetic A^{2+} cations (A^{2+} = Mn, Fe, Co, Ni, Cu) follow a similar trend as their chalcogenide counterparts with nonmagnetic A^{2+} ions, i.e., the transition pressure is proportional to the magnitude of the Cr-Cr magnetic exchange interactions active in these compounds. Therefore, we have reached the conclusion that knowing the Cr-Cr magnetic exchange interactions alone suffices to account for the high-pressure behavior of these systems. It would be interesting to search for analogous interrelations of magnetic and structural properties in relevant material families.

ACKNOWLEDGMENTS

We would like to thank Dr. D. Popov for his assistance with the XRD measurements, and Dr. S. Tkachev at GeoSoilEnviroCARS (Sector 13), APS-ANL for his assistance with the DAC gas loading. Portions of this work were performed at HPCAT (Sector 16), Advanced Photon Source (APS), Argonne National Laboratory. HPCAT operations are supported by DOE-NNSA under Award No. DE-NA0001974 and DOE-BES under Award No. DE-FG02-99ER45775, with partial instrumentation funding by NSF. The Advanced Photon Source is a U.S. Department of Energy (DOE) Office of Science User Facility operated for the DOE Office of Science by Argonne National Laboratory under Contract No. DE-AC02-06CH11357. Portions of this work were performed at GeoSoilEnviroCARS (The University of Chicago, Sector 13), APS, Argonne National Laboratory. GeoSoilEnviroCARS is supported by the National Science Foundation - Earth Sciences (Grant No. EAR-1128799) and Department of Energy- Geo-Sciences (Grant No. DE-FG02-94ER14466). This research used resources of the Advanced Photon Source, a U.S. DOE Office of Science User Facility operated for the DOE Office of Science by Argonne National Laboratory under Contract No. DE-AC02-06CH11357. Use of the COMPRES-GSECARS gas-loading system was supported by COMPRES under NSF Cooperative Agreement No. EAR 11–57758 and by GSECARS through NSF Grant No. EAR-1128799 and DOE Grant No. DE-FG02-94ER14466. This research used resources of the Advanced Photon Source, a U.S. DOE Office of Science User Facility operated for the DOE Office of Science by Argonne National Laboratory under Contract No. DE-AC02-06CH11357. We are grateful to the Michigan Space Grant Consortium for supporting this research. We acknowledge use of computational resources from the Tandy Supercomputing Center and the Ohio Supercomputing Center [71]. We acknowledge support from the NSF Grants No. CMMI 1629239. This research has been partially supported by the Deutsche Forschungsgemeinschaft (DFG) via the Transregional Collaborative Research Center TRR 80 (Augsburg-Munich).

I.E. and I.K. contributed equally to this work.

[1] P. K. Baltzer, P. J. Wojtowicz, M. Robbins, and E. Lopatin, Phys. Rev. **151**, 367 (1966).
[2] D. H. Lyons, T. A. Kaplan, K. Dwight, and N. Menyuk, Phys. Rev. **126**, 540 (1962).
[3] T. Rudolf, C. Kant, F. Mayr, J. Hemberger, V. Tsurkan, and A. Loidl, New J. Phys. **9**, 76 (2007).
[4] D. Das and S. Ghosh, J. Phys. D Appl. Phys. **48**, 425001 (2015).
[5] J. B. Goodenough, *Magnetism and the Chemical Bond* (John Wiley and Sons, New York, 1963).
[6] J. B. Goodenough, Phys. Rev. **117**, 1442 (1960).
[7] J. B. Goodenough, J. Phys. Chem. Solids **6**, 287 (1958).
[8] D. G. Wickham and J. B. Goodenough, Phys. Rev. **115**, 1156 (1959).
[9] J. D. Dunitz and L. E. Orgel, J. Phys. Chem. Solids **3**, 20 (1957).
[10] J. B. Goodenough and A. L. Loeb, Phys. Rev. **98**, 391 (1955).
[11] S. Blanco-Canosa, F. Rivadulla, V. Pardo, D. Baldomir, J.-S. Zhou, M. Garcia-Hernandez, M. A. Lopez-Quintela, J. Rivas, and J. B. Goodenough, Phys. Rev. Lett. **99**, 187201 (2007).
[12] H. Ueda and Y. Ueda, Phys. Rev. B **77**, 224411 (2008).
[13] S. Rahman, S. Samanta, D. Errandonea, S. Yan, K. Yang, J. Lu, and L. Wang, Phys. Rev. B **95**, 024107 (2017).
[14] P. Kistaiah, K. S. Murthy, and K. V. K. Rao, J. Less-Common Met. **98**, L13 (1984).
[15] S.-D. Guo and B.-G. Liu, J. Phys.: Condens. Matter **24**, 45502 (2012).
[16] Y. Amiel, G. K. Rozenberg, N. Nissim, A. Milner, M. P. Pasternak, M. Hanfland, and R. D. Taylor, Phys. Rev. B **84**, 224114 (2011).
[17] S. Rahman, H. Saqib, J. Zhang, D. Errandonea, C. Menendez, C. Cazorla, S. Samanta, X. Li, J. Lu, and L. Wang, Phys. Rev. B **97**, 174102 (2018).
[18] C. Ederer and M. Komelj, Phys. Rev. B **76**, 064409 (2007).
[19] I. Efthimiopoulos, T. Lochbiler, V. Tsurkan, A. Loidl, V. Felea, and Y. Wang, J. Phys. Chem. C **121**, 769 (2017).
[20] I. Efthimiopoulos, Z. T. Y. Liu, M. Kucway, S. V. Khare, P. Sarin, V. Tsurkan, A. Loidl, and Y. Wang, Phys. Rev. B **94**, 174106 (2016).
[21] I. Efthimiopoulos, A. Yaresko, V. Tsurkan, J. Deisenhofer, A. Loidl, C. Park, and Y. Wang, Appl. Phys. Lett. **103**, 201908 (2013).
[22] I. Efthimiopoulos, A. Yaresko, V. Tsurkan, J. Deisenhofer, A. Loidl, C. Park, and Y. Wang, Appl. Phys. Lett. **104**, 11911 (2014).

[23] I. Efthimiopoulos, Z. T. Y. Liu, S. V. Khare, P. Sarin, V. Tsurkan, A. Loidl, D. Popov, and Y. Wang, Phys. Rev. B **93**, 174103 (2016).

[24] I. Efthimiopoulos, V. Tsurkan, A. Loidl, D. Zhang, and Y. Wang, J. Phys. Chem. C **121**, 16513 (2017).

[25] K. Dey, S. Majumdar, and S. Giri, Phys. Rev. B **90**, 184424 (2014).

[26] J. Barman, T. Bora, and S. Ravi, J. Magn. Magn. Mater. **385**, 93 (2015).

[27] K. Syassen, High Pressure Res. **28**, 75 (2008).

[28] D. Zhang, P. K. Dera, P. J. Eng, J. E. Stubbs, J. S. Zhang, V. B. Prakapenka, and M. L. Rivers, J. Visualized Exp. **119**, e54660 (2017).

[29] P. W. Stephens, J. Appl. Crystallogr. **32**, 281 (1999).

[30] R. B. von Dreele, J. Appl. Crystallogr. **30**, 517 (1997).

[31] G. Kresse and J. Furthmüller, Comput. Mater. Sci. **6**, 15 (1996).

[32] G. Kresse and J. Furthmüller, Phys. Rev. B **54**, 11169 (1996).

[33] G. Kresse and J. Hafner, Phys. Rev. B **49**, 14251 (1994).

[34] G. Kresse and J. Hafner, Phys. Rev. B **47**, 558 (1993).

[35] G. Kresse and D. Joubert, Phys. Rev. B **59**, 1758 (1999).

[36] P. E. Blöchl, Phys. Rev. B **50**, 17953 (1994).

[37] J. P. Perdew, J. A. Chevary, S. H. Vosko, K. A. Jackson, M. R. Pederson, D. J. Singh, and C. Fiolhais, Phys. Rev. B **46**, 6671 (1992).

[38] L. Wang, T. Maxisch, and G. Ceder, Phys. Rev. B **73**, 195107 (2006).

[39] A. Jain, G. Hautier, S. P. Ong, C. J. Moore, C. C. Fischer, K. A. Persson, and G. Ceder, Phys. Rev. B **84**, 045115 (2011).

[40] A. van de Walle, P. Tiwary, M. de Jong, D. L. Olmsted, M. Asta, A. Dick, D. Shin, Y. Wang, L.-Q. Chen, and Z.-K. Liu, CALPHAD: Comput. Coupling Phase Diagrams Thermochem. **42**, 13 (2013).

[41] A. Zunger, S. H. Wei, L. G. Ferreira, and J. E. Bernard, Phys. Rev. Lett. **65**, 353 (1990).

[42] A. van de Walle, M. Asta, and G. Ceder, CALPHAD: Comput. Coupling Phase Diagrams Thermochem. **26**, 539 (2002).

[43] A. van de Walle, CALPHAD: Comput. Coupling Phase Diagrams Thermochem. **33**, 266 (2009).

[44] I. Efthimiopoulos, J. Kemichick, X. Zhou, S. V. Khare, D. Ikuta, and Y. Wang, J. Phys. Chem. A **118**, 1713 (2014).

[45] I. Efthimiopoulos, Z. T. Y. Liu, S. V. Khare, P. Sarin, T. Lochbiler, V. Tsurkan, A. Loidl, D. Popov, and Y. Wang, Phys. Rev. B **92**, 064108 (2015).

[46] See Supplemental Material at http://link.aps.org/supplemental/10.1103/PhysRevB.97.184435 for the complete set of experimental and calculated structural parameters, as well as the list of magnetic data used for our DFT calculations. An overview table for all relevant spinels is also supplied for convenience.

[47] S. Klotz, J.-C. Chervin, P. Munsch, and G. Le Marchand, J. Phys. D: Appl. Phys. **42**, 75413 (2009).

[48] W. Yong, S. Botis, S. R. Shieh, W. Shi, and A. C. Withers, Phys. Earth Planet. Inter. **196–197**, 75 (2012).

[49] F. Birch, Phys. Rev. **71**, 809 (1947).

[50] F. Birch, J. Geophys. Res. **83**, 1257 (1978).

[51] K. Tomiyasu, J. Fukunaga, and H. Suzuki, Phys. Rev. B **70**, 214434 (2004).

[52] S. Baroni, S. de Gironcoli, A. D. Corso, and P. Giannozzi, Rev. Mod. Phys. **73**, 515 (2001).

[53] Z.-Y. Li, X. Li, J.-G. Cheng, L. G. Marshall, X.-Y. Li, A. M. dos Santos, W.-G. Yang, J. J. Wu, J.-F. Lin, G. Henkelman, T. Okada, Y. Uwatoko, H. B. Cao, H. D. Zhou, J. B. Goodenough, and J.-S. Zhou, Phys. Rev. B **94**, 165159 (2016).

[54] P. G. Radaelli, New J. Phys. **7**, 53 (2005).

[55] M. R. Suchomel, D. P. Shoemaker, L. Ribaud, M. C. Kemei, and R. Seshadri, Phys. Rev. B **86**, 054406 (2012).

[56] M. Schmidt, W. Ratcliff, II, P. G. Radaelli, K. Refson, N. M. Harrison, and S. W. Cheong, Phys. Rev. Lett. **92**, 056402 (2004).

[57] J. Ruiz-Fuertes, A. Friedrich, J. Pellicer-Porres, D. Errandonea, A. Segura, W. Morgenroth, E. Haussuhl, C.-Y. Tu, and A. Polian, Chem. Mater. **23**, 4220 (2011).

[58] J. Ruiz-Fuertes, A. Segura, F. Rodriguez, D. Errandonea, and M. N. Sanz-Ortiz, Phys. Rev. Lett. **108**, 166402 (2012).

[59] I. Loa, P. Adler, A. Grzechnik, K. Syassen, U. Schwarz, M. Hanfland, G. K. Rozenberg, P. Gorodetsky, and M. P. Pasternak, Phys. Rev. Lett. **87**, 125501 (2001).

[60] F. Rivadulla, M. Banobre-Lopez, C. X. Quintela, A. Pineiro, V. Pardo, D. Baldomir, M. A. Lopez-Quintela, J. Rivas, C. A. Ramos, H. Salva, J.-S. Zhou, and J. B. Goodenough, Nat. Mater. **8**, 947 (2009).

[61] I. Efthimiopoulos, Ph.D. thesis, Aristotle University of Thessaloniki, Thessaloniki, Greece, 2010.

[62] B. C. Melot, J. E. Drewes, R. Seshadri, E. M. Stoudenmire, and A. P. Ramirez, J. Phys.: Condens. Matter **21**, 216007 (2009).

[63] E. Winkler, S. Blanco Canosa, F. Rivadulla, M. A. López-Quintela, J. Rivas, A. Caneiro, M. T. Causa, and M. Tovar, Phys. Rev. B **80**, 104418 (2009).

[64] W. M. Xu, G. R. Hearne, S. Layek, D. Levy, J.-P. Itie, M. P. Pasternak, G. K. Rozenberg, and E. Greenberg, Phys. Rev. B **95**, 045110 (2017).

[65] A. Kyono, S. A. Gramsch, T. Yamanaka, D. Ikuta, M. Ahart, B. O. Mysen, H. K. Mao, and R. J. Hemley, Phys. Chem. Miner. **39**, 131 (2012).

[66] F. J. Manjon and R. I. Vilaplana, *Pressure-Induced Phase Transitions in AB2 × 4 Chalcogenide Compounds* (Springer-Verlag, Berlin, 2014).

[67] D. Errandonea, R. S. Kumar, F. J. Manjon, V. V Ursaki, and I. M. Tiginyanu, J. Appl. Phys. **104**, 63524 (2008).

[68] D. Louer and R. Vargas, J. Appl. Crystallogr. **15**, 542 (1982).

[69] A. Kismarahardja, J. S. Brooks, A. Kiswandhi, K. Matsubayashi, R. Yamanaka, Y. Uwatoko, J. Whalen, T. Siegrist, and H. D. Zhou, Phys. Rev. Lett. **106**, 056602 (2011).

[70] D. B. Rogers, R. J. Arnott, A. Wold, and J. B. Goodenough, J. Phys. Chem. Sol. **24**, 347 (1963).

[71] Ohio Supercomputer Center, http://osc.edu/ark:/19495/f5s1ph73